

Impact of Graphitization Degree on the Electrochemical and Thermal Properties of Coal

Xiang Xu, Daiyong Cao,* Yingchun Wei, Anmin Wang, Gaojian Chen, Tianyuan Wang, Guixiang Wang, and Xinli Chen



Cite This: *ACS Omega* 2024, 9, 2443–2456



Read Online

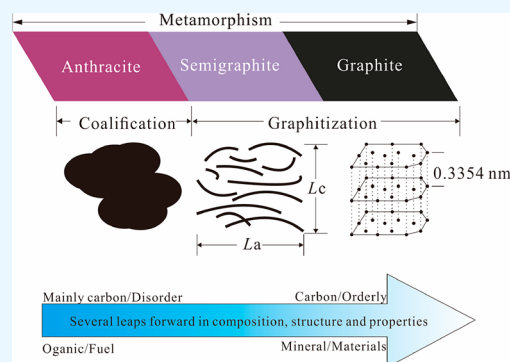
ACCESS |

Metrics & More

Article Recommendations

Supporting Information

ABSTRACT: Coal-based cryptocrystalline graphite is an intermediate phase formed during the transformation of highly metamorphic anthracite into crystalline graphite. In order to explore the relationship between the graphitization degree of coal-based cryptocrystalline graphite and its physical properties from macromolecular structure to provide a theoretical basis for industrial application, samples were tested by X-ray diffraction, electrochemistry, and thermal conductivity and compared with standard graphite (SG) and artificial thermal simulation graphitized samples. The results show that with the increase of graphitization degree and the growth of microcrystalline structure, the electrical impedance of cryptocrystalline graphite decreases, the conductivity increases, the specific capacity of initial discharge increases, and the thermal conductivity increases, which gradually approach the electrical and thermal properties of crystalline graphite. The linear equations between impedance and L_a and L_c are $y = -0.42x + 70.44$ and $y = -1.87x + 70.62$, and the correlation coefficients are 0.93 and 0.88. The linear equations between thermal conductivity and the horizontal extension length (L_a) and vertical stacking thickness (L_c) are $y = 0.09x + 1.36$ and $y = 0.4x + 0.76$, the correlation coefficients are 0.82 and 0.84, and the reduction of microcrystalline parameters d_{002} and the increase of L_a and L_c lead to a direct improvement of physical properties. Artificial thermal simulation samples also show the same regularity, but their physical properties are lower than those of natural evolution samples. Short-term high-temperature simulation is different from long-term magma heat and pressure, and the growth of graphite microcrystals is more complete under long-term geological conditions, resulting in better physical properties.



1. INTRODUCTION

Graphite, an isomer of carbon, possesses a distinctive laminar structure and exhibits unique properties, such as lubricity, excellent thermal and electrical conductivity, high- and low-temperature resistance, radiation resistance, and chemical stability. These unique properties make graphite widely used in various sciences, technologies, and engineering fields. Additionally, its wide range of applications, deep processing products with high added value, and long industrial chain contribute to graphite's status as an indispensable strategic material.^{1–3} In 2018, the United States of America (USA) identified graphite as one of the 35 “key minerals”, while the International Energy Agency predicted a 25-fold increase in graphite demand by 2040 compared to 2021, in a sustainable development scenario.⁴ Furthermore, China’s “National Mineral Resources Plan (2016–2020)” included graphite and 24 other minerals as strategic minerals for the first time.

According to the degree of development of the graphite crystal structure, graphite can be categorized into two types: crystalline and cryptocrystalline (microcrystalline). Cryptocrystalline graphite exhibits varying degrees of development in its microcrystalline structure, sharing similar physical character-

istics with crystalline graphite.⁵ Research shows that most cryptocrystalline graphite is formed during the graphitization stage of coal subjected to magmatic thermal metamorphism and tectonic stress.^{6,7} Cryptocrystalline graphite serves as the primary component of coal-based graphite and predominantly consists of an apocrystalline or microcrystalline structure. It is composed of a combination of newly formed components with different degrees of graphitization and residual coal and rock components. The formation of cryptocrystalline graphite occurs through the coevolution of coal graphitization and coalification with continuous progress and several jumps. The degree of graphitization increased during the whole process. Microscopically, this evolution is manifested as the gradual formation of graphite structures with different degrees of order, transitioning from organic components to graphite minerals

Received: September 9, 2023

Revised: October 22, 2023

Accepted: December 7, 2023

Published: January 2, 2024



with three-dimensional (3D) crystal structures.⁸ Graphite is considered the final stage of this evolution.^{9,10} With the progress of graphitization, the carbon structure gradually changed from the amorphous shape in anthracite to the 3D ordered structure of graphite. And it changes from a short and disordered messy layer to a long and ordered layered arrangement, the gap between layers decreases continuously, and the horizontal extension and vertical stacking degree increase.^{11–13} Zeng et al. also found through high-temperature thermal simulation graphitization that the graphite crystal layer spacing gradually decreased and the degree of stacking and extension increased.¹⁴ In fact, cryptocrystalline graphite is an intermediate phase in the transition from highly metamorphic anthracite to graphite crystals. On the nanoscale, it appears as a disordered organic component, with its macromolecular structure evolving into an ordered 3D spatial crystal structure of graphite. The evolution of macromolecular structure results in different degrees of graphitization, determining the transitional and complex physical properties exhibited by different types of coal measures graphite.^{15,16} Consequently, the physical properties of cryptocrystalline graphite tend to exhibit transitional properties similar to mineral graphite.

Previous studies of the structure and evolution of cryptocrystalline graphite have yielded fruitful results. This includes understanding the evolution of macromolecular structure during the transition from high-metamorphic anthracite to graphite, identifying the characteristics of cryptocrystalline graphite, and studying the controlling factors in its genesis.^{17–19} In terms of the electrical properties, the theoretical electrical capacity of graphite is ~ 372 mAh/g. However, recent findings have shown that nongraphite carbon materials, such as amorphous carbon, possess a theoretical lithium storage capacity surpassing that of graphite.^{20–22} Many scholars have focused on purifying and modifying cryptocrystalline graphite using a high temperature to improve the degree of graphitization to enhance its performance as an electrode material. These treatments have resulted in a higher specific capacity of graphite materials.^{23–25} Previous studies have shown that the higher the degree of graphitization, the larger the specific capacity of graphite as a lithium ion anode material.^{26–31} Lin et al. found that the microcrystalline structure of carbon materials has a strong correlation with its potassium ion storage performance.³² Moreover, it has been observed that a high degree of graphitization and an orderly arrangement of carbon atoms contribute to an increased capacity for lithium embedded in carbon materials.³³ In terms of thermal properties, Zhao et al.³⁴ summarized the thermal conductivity of graphite materials based on different testing methods employed by previous studies. The thermal conductivities of graphite materials tested in parallel and vertical layers are ~ 2000 and ~ 5 W/(m K), respectively. Although slight variations exist in the thermal conductivity values obtained using different testing methods, the overall differences are not significant.^{35–39} By adding cryptocrystalline graphite as a porous matrix, the composite phase change materials has higher thermal conductivity.⁴⁰ Qiu et al.⁴¹ used X-ray diffraction (XRD) analysis to examine the influence of microcrystalline parameters (d_{002} and L_a) variation on thermal conductivity.

Compared to crystalline graphite, cryptocrystalline graphite possesses characteristics, such as concentrated ore bodies, high-grade deposits, and easy development and can serve as a partial substitute for crystalline graphite. Recently, there has

been a growing demand and consumption of graphite, depleting crystalline graphite resources. Therefore, developing and using cryptocrystalline graphite will remarkably alleviate the pressure on the demand for crystalline graphite resources. However, due to the lack of a corresponding theoretical basis, the understanding of its basic physical properties and the difference of physical properties between different degrees of graphitization are seriously insufficient. At present, the application is mainly based on raw ore and original processing products,⁴² such as metallurgy, electrical, refractory materials, batteries, and other fields, with low added value of products. And often mixed with coal, resulting in a lot of waste of resources. Therefore, strengthening research on the internal relationship between the degree of graphitization of cryptocrystalline and its physical properties and revealing the change law of the physical properties of cryptocrystalline graphite during the evolution of macromolecular structure provide a new application direction for cryptocrystalline graphite with different degrees of graphitization and have great significance for the industrial application of cryptocrystalline graphite, which also provides a new direction and basis for new carbon materials. It also has great significance for new electrochemical energy storage and thermal interface materials. It provides the experimental basis for promoting the application of coal measure cryptocrystalline graphite in the field of new energy and new materials and realizing the strategic substitution of crystalline graphite.

Herein, the relationship between the microcrystalline structure and electrical and thermal properties of cryptocrystalline graphite at different graphitization stages was studied. XRD was used to analyze the graphite crystal parameters at different graphitization stages. And the electrical and thermal properties were tested at each graphitization stage. The relationship between microcrystalline parameters and physical properties was analyzed qualitatively and quantitatively. The study will provide insight into the electrical and thermal properties corresponding to different graphitization degrees from the perspective of macromolecular structure evolution.

2. EXPERIMENT

2.1. Experimental Sample. In this study, a series of samples with different degrees of graphitization was collected from a typical cryptocrystalline graphite mining area in Hunan, Southern China. In order to avoid the difference of samples under different natural conditions, the samples were taken from the same coal seam in the Lutang mining area. The obtained samples were tested by X-ray diffraction, and ten samples with different degrees of graphitization were selected according to the results. The samples were labeled as Z1, Z2, Z3, Z4, Z5, Z6, Z7, Z8, Z9, and Z10. Table 1 presents the basic information on these samples.

At the same time, a standard graphite sample (SG) of Henan crystalline graphite ore was subjected to the same experiment to compare with the naturally evolved graphite sample.

2.2. Sample Treatment. Samples were demineralized to eliminate the influence of the mineral composition on the test results. First, the samples were crushed and passed through a 200-mesh (75 μm) standard sieve. Wet particle size analysis was performed using the Malvern Mastersizer 3000 laser particle size analyzer produced in the U.K. The particle size distribution of the sample is shown in Table 2. It can be seen that the average particle size of most samples is less than 75 μm , more than 90% of each sample is less than 75 μm , more

Table 1. Basic Information of Samples

No.	Site	FC _{ad} /% ^a	Md/% ^a	A _{ad} /% ^a	V _{daf} /% ^a
Z1	Lutang mine	83.73	0.91	12.09	4.18
Z2	Lutang mine	73.57	0.36	23.51	2.92
Z3	Lutang mine	84.87	0.42	10.71	4.42
Z4	Lutang mine	83.30	0.60	11.78	4.92
Z5	Lutang mine	81.37	0.42	16.24	2.39
Z6	Lutang mine	70.48	0.92	25.24	4.28
Z7	Lutang mine	87.93	0.54	7.81	4.26
Z8	Lutang mine	88.54	1.14	6.92	4.54
Z9	Lutang mine	86.40	2.02	10.24	3.36
Z10	Lutang mine	84.00	0.28	11.10	4.90

^aFC_{ad}, fixed carbon; Md, moisture; A_{ad}, ash content; V_{daf}, volatile matter.

Table 2. Sample Particle Size Distribution

No.	Distribution (%) for given particle size		Dv(10) / μm^a	Dv(50) / μm^a	Dv(90) / μm^a
	<75 μm	>75 μm			
Z1	96.85	3.15	3.38	9.45	43.6
Z2	94.52	5.48	3.62	11.2	56.5
Z3	93.83	6.17	3.50	9.90	57.8
Z4	85.69	14.31	3.74	13.9	139
Z5	93.07	6.93	4.55	13.0	64.1
Z6	90.37	9.63	2.60	12.5	74.2
Z7	82.19	17.81	3.70	23.1	130
Z8	92.06	7.94	3.06	14.6	68.6
Z9	84.88	15.12	2.95	25.0	93.5
Z10	85.85	14.15	2.39	24.4	89.2

^aDv(10), particles measured in 10% of the sample are smaller than this particle size; Dv(50), particles measured in 50% of the sample are smaller than this particle size; Dv(90), particles measured in 90% of the sample are smaller than this particle size.

than 50% is less than 20 μm , and the samples can meet the 200-mesh.

Each 15 g of pulverized coal was mixed with 80 mL of HCl (36% mass fraction) solution in a plastic beaker. The HCl solution was stirred in a constant temperature bath at 60 °C for 4 h and then filtered. Then, 80 mL of HF (hydrofluoric acid) solution with a mass fraction of 40% was added to the sample, and the pickling process was repeated using the same water bath. Two acids are used to dissolve inorganic minerals in the sample. Finally, the residual coal sample was cleaned and filtered with ultrapure water. Add 50% AgNO₃ solution to remove excess acids and chlorides from the filtrate until there is no precipitation. The pickling coal sample was filtered using filter paper and put in the oven for vacuum drying at 6 °C for 24 h to obtain the demineralized coal sample.

2.3. High-Temperature Simulation. In order to study the relationship between the physical properties of different graphitization degrees of aphanitic graphite in coal measures under natural conditions, samples with the same mining area, geological background, and evolutionary path were selected for experiments. At the same time, the effects of primary minerals were excluded from the sample de-ashing treatment. However, in order to minimize the influence of natural factors on its physical properties, the same sample was selected to control its graphitization degree through high-temperature thermal simulation so as to simulate the change of physical properties,

under different graphitization degrees and compare with the natural evolution sequence.

A sample with low metamorphic bituminous coal (FC_{ad} = 65.01%; V_{daf} = 30.85%) were subjected to high-temperature thermal simulation to change their graphitization degree. The same experiments were performed on the obtained samples and compared with those on the naturally evolved samples. In this experiment, NTG-SML-60W integrated laboratory graphitization furnace was used, and the manufacturer was Zhuzhou Nuotian Electric Heating Technology Co., Ltd. The specific experimental steps are as follows: 15 g of coal sample is put into each vessel, placed in the graphitization furnace, and vacuumed to replace the gas once before heating, and argon gas with a flow rate of 10 L/min is used to protect the whole experiment. The experiment adopts a segmented heating method: First, under the condition of heating rate of 5 °C/min, the temperature is raised to 1000 °C and the heat is kept for 60 min. Then the temperature is raised to the target temperature point at a rate of 10 °C/min, held for 90 min, and finally cooled to room temperature naturally. Four temperature points were set at 1800, 2100, 2400, and 2700 °C; the samples obtained after heating were recorded as ND18, ND21, ND24, and ND27 in turn.

2.4. X-ray Diffraction. XRD is an effective method for studying crystal structure and is widely used in the analysis of coal-graphite structures. In addition, the important parameters of microcrystalline structure can be obtained using XRD analysis.⁴³ XRD analysis was used in this study to determine the degree of graphitization. Prior to testing, the samples were crushed to 200 mesh and then demineralized. The XRD instrument used was the SmartLab-9 kW with a copper target from Rigaku Co. of the United States, with an accelerated voltage of 45 kV, current of 200 mA, scanning range of 2 θ from 5 to 70°, and scanning rate of 2°/min. The obtained data were processed using JADE software, and the carbon layer spacing d_{002} was calculated using the Bragg equation.⁴⁴

$$d_{002} = \lambda / (2 \sin \theta) \quad (1)$$

The degree of graphitization was calculated using MERING and MARIE(1958) to optimize Franklin's model:⁴⁵

$$g = (0.3440 - d_{002}) / (0.3440 - 0.3354) \quad (2)$$

The horizontal extension length (L_a) and vertical stacking thickness (L_c) of the carbon layer were calculated by using the Schieler formula. The number of stacking layers was obtained through stacking thickness and layer spacing.

$$L_a = (k_1 \lambda) / [\beta(100) \cos \theta(100)] \quad (3)$$

$$L_c = (k_2 \lambda) / [\beta(002) \cos \theta(002)] \quad (4)$$

Here, β is the revised half-height width, and k_1 and k_2 are 1.84 and 0.89, respectively.

2.5. Electrochemical Test. Graphite has been extensively studied as a carbon material for lithium-ion battery electrodes. Many scholars have used graphite for electrochemical testing by making lithium-ion batteries to test their electrochemical performance.^{46–49} In this study, a liquid lithium-ion battery was used for electrochemical testing to examine electrochemical impedance and charge–discharge cycle. The electrochemical impedance reflects conductivity, while battery charging and discharging reflect the lithium storage and discharge capacities of the sample.

A mixture of 0.8 g of cryptocrystalline graphite, 0.1 g of acetylene black (SuperP), and 0.1 g of poly(vinylidene fluoride) (PVDF) was added to 3 mL of *N*-methyl-2-pyrrolidone (NMP) to create a homogeneous solution. SuperP is produced by China Delong Chemical Co., Ltd. It has the characteristics of high purity, low heavy metal content, and strong electrical conductivity and is mixed with graphite to enhance electrical conductivity. PVDF is produced by the French Arkema company, is soluble in strong polar solvents and nonconductive, and is used as a positive electrode binder. NMP, a colorless transparent liquid, is produced by China Changxin Chemical and used as a solvent to fuse PVDF, graphite, and carbon black together, so that the binder and other substances are fully mixed and evenly distributed. The solution was mixed and stirred on an electromagnetic stirring table for 12 h. Then, a copper foil was evenly scraped with a 25 μm blade (Figure 1a). After 12 h of drying in an oven at 90 $^{\circ}\text{C}$,



Figure 1. (a) Graphite mixed solution on copper sheet; (b) CR2032 button cells; (c) impedance tester; (d) electrochemical workstation.

the copper foil was cut into round sheets with a diameter of 1 cm and prepared as CR2032 button cells (Figure 1b). The entire process was conducted under anaerobic conditions to prevent the oxidation of the lithium plates. After 12 h, the

resistance was tested using a resistivity tester made by Zahner GMBH in Germany (Figure 1c). Charge and discharge of the battery were analyzed using the Lanhe system of China Landian Electronics Co., Ltd. (Figure 1d). Figure 2 shows the block diagram of the electrochemical test system and the battery structure diagram.

2.6. Thermal Conductivity Test. Due to the high anisotropy of graphite, there is a large difference in thermal conductivity between its surfaces. Since the sample in this study did not possess a complete graphite structure and contained an amorphous molecular structure with an incomplete crystal form, the sample could exhibit low thermal conductivity.⁵⁰ In addition, since the sample was in powder form, it cannot be tested for anisotropy. Therefore, the overall thermal conductivity was measured by using the transient plane heat source method.

The experimental instrument used was the Hot Disk TPS 2500S thermal conductivity tester produced in Germany. The powder sample was tested at 25 $^{\circ}\text{C}$ using a nickel probe with a radius of 6.394 mm. The powder sample was compressed at 20 MPa to form two pieces, each with a thickness of 30 mm and a diameter of 50 mm. The Hot Disk probe was placed inside the sample to maintain flatness during transient recording, and then, the sample was inserted into the container. The initial heating power of the probe was set at 0.3 W, and the temperature increase (Δt) of each sample was recorded. The thermal conductivity was calculated by using the Fourier diffusion thermal conductivity equation:

$$K = QH/\Delta tS \quad (5)$$

Here, K is the thermal conductivity (unit, $\text{W}/(\text{m K})$); Q is the initial power (unit, W); H is the sample thickness (unit, m); Δt is the temperature rise, in kelvin (K); and S is the sample area (unit, m^2).

3. EXPERIMENTAL RESULTS

The experimental results of natural evolution samples and artificial thermal simulation samples are shown in Supporting Information Table S1.

3.1. X-ray Diffraction Characteristics. According to the XRD test results, the microcrystalline parameters d_{002} , L_a , and L_c of graphite were calculated, and the graphitization degree of

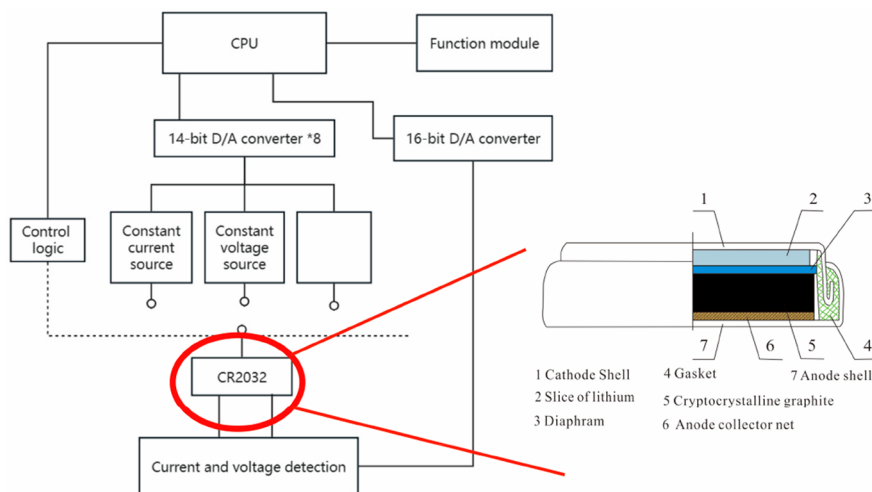


Figure 2. Block diagram of electrochemical test system and battery structure diagram.

each sample was calculated. According to the coal measure graphite division scheme,¹⁵ the samples were categorized into three grades: graphite, semigraphite, and anthracite.

Figure 3 shows the XRD characteristics of the samples. An evident graphite-002 peak is observed around $2\theta = 26^\circ$ of the samples.

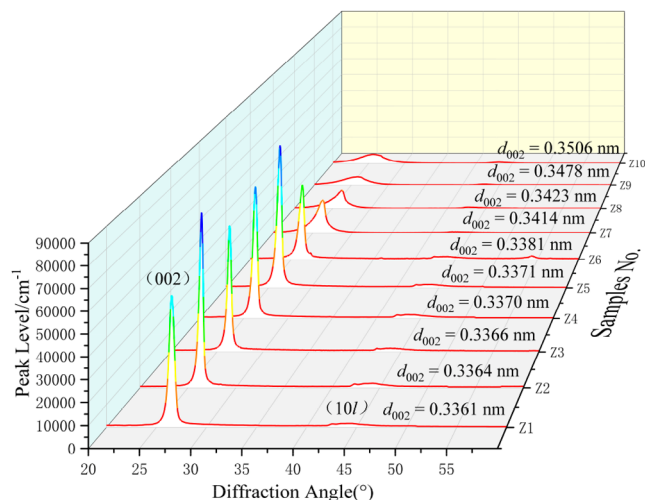


Figure 3. XRD characteristic pattern.

From Z10 to Z1, the 002 peak gradually sharpens, the half-height width decreases, and the peak shape becomes symmetrical. This indicates a gradual increase in the graphitization degree and the appearance of a graphite structure in the samples. The 002 peaks of Z10, Z9, Z8, and Z7 exhibit strong asymmetry, symbolizing the turbostratic structure of anthracite. The 10l band remains unsplit, suggesting a wide and slow diffraction. This indicates that the samples still possess polycyclic aromatic hydrocarbon structures (PHAs) of anthracite. For Z6, Z5, and Z4, the 002 peak becomes higher and sharper, indicating a higher degree of metamorphism than Z10 to Z7 and the degree of graphite crystallization significantly increased. The 002 diffraction peaks of Z3, Z2, and Z1 are further reduced and narrowed compared to those of Z5 and Z4. Although the peak heights of Z1 and Z3 are lower, their peak shapes are sharper, and the half-height width is narrower. The degree of crystallization of graphite is not different from that of Z2, but the graphite structure is more regular than those of Z5 and Z4. The half-height width of Z5 to Z1 gradually decreased and tended toward symmetry. Notably, Z3, Z2, and Z1 exhibit sharp and symmetrical crystal peaks, indicating the presence of a graphite crystal structure in the samples. The 10l band from Z5 to Z1 gradually starts to split into 100 and 101 peaks, and the structure of the sample changed from PAHs to the carbon atom lattice structure of graphite.

Compared with the XRD pattern of the graphite sample (Figure 4), it can be seen that the standard graphite sample has a very sharp (002) peak, which can reach more than 400000 cm^{-1} . The half-height width is small, and the peak shape is symmetrical, indicating that it has a complete graphite structure.

By analyzing the microcrystalline layer spacing (d_{002}) from Z10 to Z1, it can be observed that d_{002} decreases and the graphitization degree of the sample increases. As shown in Figure 5, microcrystalline parameters L_a and L_c gradually

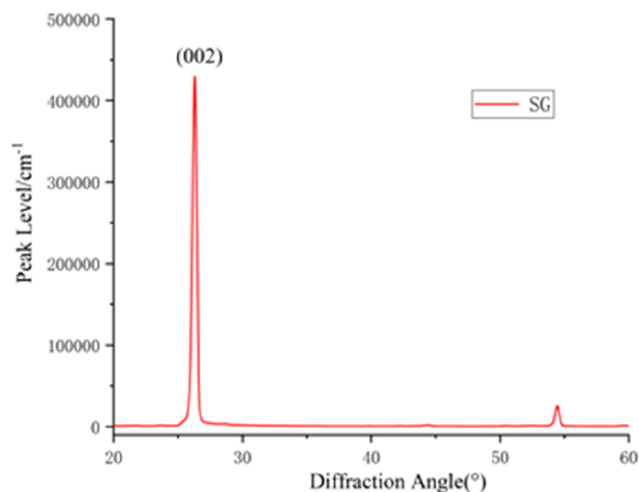


Figure 4. XRD pattern of standard graphite.

increase with the decrease of layer spacing d_{002} and basic structural units form rapidly with the increase of graphitization degree, indicating the rapid formation of the graphite crystal structure.

3.2. Impedance. Impedance ($Z(\omega)$) is composed of two parts: the real part on the horizontal axis and the imaginary part on the vertical axis. The impedance test results correspond to the dispersions of the real and imaginary parts of the internal resistance, which are plotted as the electrochemical impedance spectrum. Electrochemical impedance spectroscopy (EIS) is an electrochemical system that simplifies a battery into multiple electronic components, and the spectrum from left to right is the conversion from low frequency to high frequency.⁵¹ The diagram shows the shape of two quasi-semicircles. The impedance of the cell is the horizontal value of the first semicircle's diameter. In order to avoid accidental errors in the experimental results and ensure the authenticity of the results, four parallel tests were carried out in the experiment.

After four parallel tests, the impedance difference of the sample is small, the average impedance of the sample is obtained, and the electrochemical impedance spectrum is drawn. As shown in Figure 6, Z9 exhibits the highest impedance of 70Ω , while Z2 exhibits the lowest impedance of 32Ω . The impedance of the graphite sample SG reached 28Ω , only 4Ω lower than that of the cryptocrystalline graphite sample Z2, only 12.5% lower, indicating that the cryptocrystalline graphite was close to graphite to a certain extent.

3.3. Specific Capacity of Initial Discharge. The average of the three test results was used as the specific capacity of the sample for the first discharge. Figure 7 shows the initial discharge capacities of the tested samples. At a current density of 0.01 mA/g , the initial discharge-specific capacity of the sample gradually increases with an increase in the degree of graphitization. Among the natural samples, Z3 exhibits the highest initial discharge-specific capacity of 1471.63 mAh/g . Z10 exhibits the lowest initial discharge capacity, at only 259.7 mAh/g . The specific discharge capacity of SG is 340.2 mAh/g , which is very close to the theoretical reserve of graphite of 372 mAh/g , and most of the tested cryptocrystalline graphite samples can be higher than this result, in line with the literature which mentioned that amorphous carbon has more theoretical lithium storage than graphite.^{20–22}

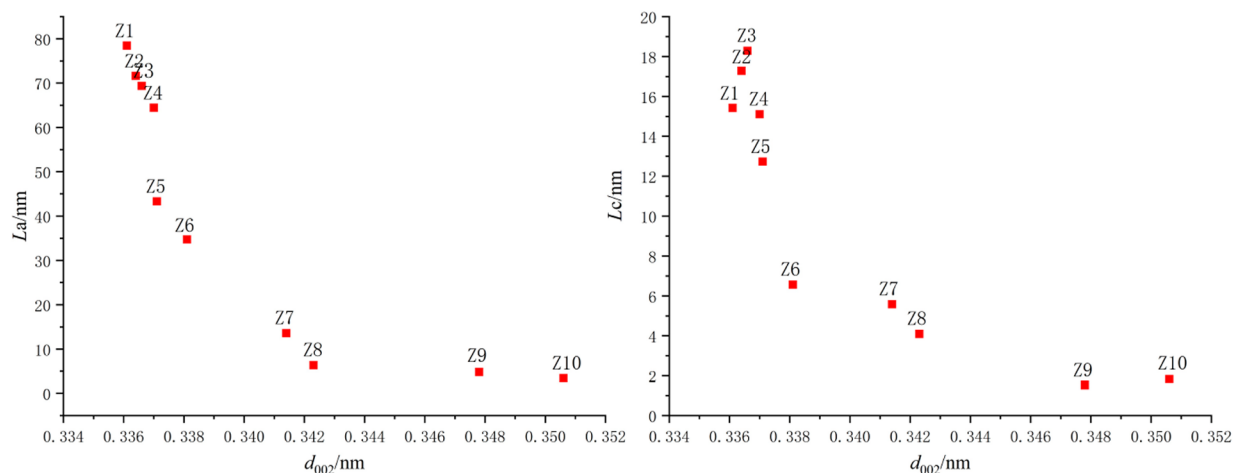


Figure 5. d_{002} - L_a scatter plot (left); d_{002} - L_c scatter plot (right).

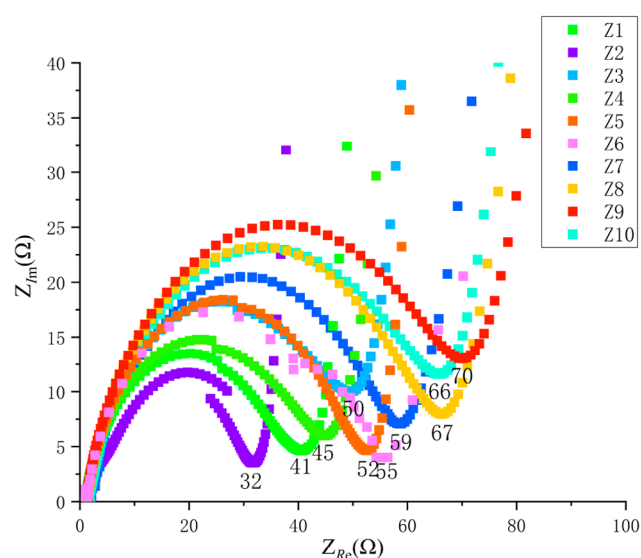


Figure 6. EIS atlas of the sample.

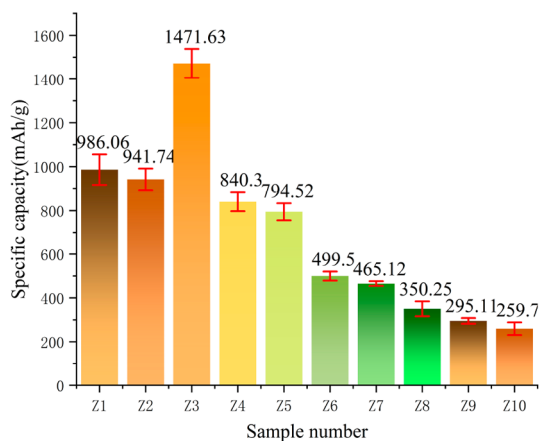


Figure 7. Discharge capacity histogram.

3.4. Thermal Conductivity. The average of the four thermal conductivity coefficients is used as the thermal conductivity coefficient of the sample, and a bar chart of the average thermal conductivity of each sample is drawn. Figure 8

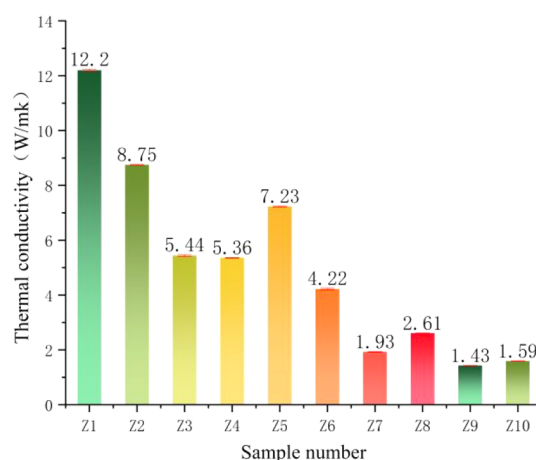


Figure 8. Thermal conductivity histogram.

shows the thermal conductivity of the samples. Generally, the thermal conductivity of the natural samples from Z1 to Z10 shows a downward trend, indicating that the overall thermal conductivity gradually increases with an increase in the degree of graphitization. Sample Z1, which exhibits the highest degree of graphitization and crystallization, has a thermal conductivity of 12.2 W/(m K), while Z9 and Z10 anthracite samples, which exhibit the lowest degree of graphitization, have the lowest thermal conductivities of 1.43 and 1.59 W/(m K), respectively. The thermal conductivity of SG can reach 19.38 W/(m K), which is a certain gap compared to cryptocrystalline graphite.

3.5. Thermal Simulation Results. The experimental results of thermal simulation samples are shown in Table S1. According to the research results of predecessors and our research group, it is difficult for the sample to reach a high degree of graphitization by heating without the catalytic action of additives.^{52–55}

As shown in Figure 9, it can be seen that, with the increase of temperature, the 002 peak shown by the XRD pattern gradually changes from low to sharp, indicating that the graphite crystal development is gradually complete. However, compared with the samples of natural evolution, the 002 peak of artificial graphitization reached a maximum of 10000 cm^{-1} , which was far lower than the development of 002 peak of natural evolution. It can be seen that the graphitized samples

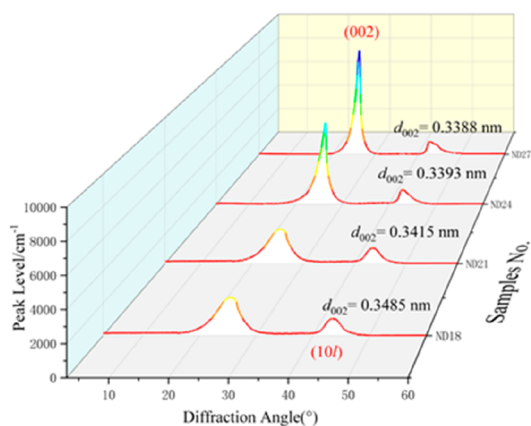


Figure 9. XRD characteristic pattern of the thermal simulation sample.

controlled by thermal simulation have great limitations and cannot reach a high degree of graphitization. This is due to short-term high-temperature simulations, which are still inferior to metamorphism under long geological conditions. It can also be seen from the microcrystalline parameters that L_a and L_c of artificially simulated samples are much smaller than those of naturally evolved samples among samples with the same graphitization degree.

As shown in Figure 10, the impedance of the sample can be seen. The impedance of ND18 is the highest at 72Ω , and the

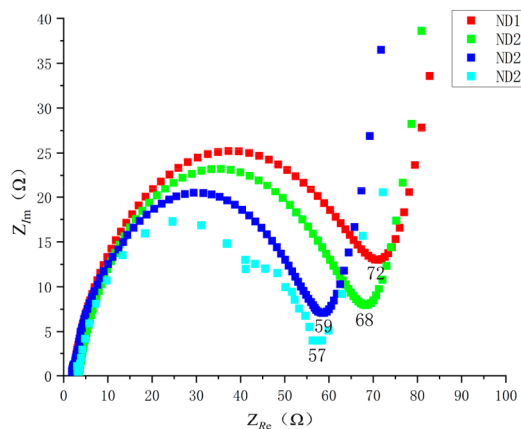


Figure 10. EIS atlas of thermal simulation samples.

impedance of ND27 is the lowest at 57Ω . With the increase of the graphitization temperature, the degree of graphitization increases and the impedance also decreases.

As shown in Figure 11, the first specific discharge capacity of the thermal simulated graphitized sample also increases with the increase in graphitization temperature. The discharge capacity of ND18 is 85.3 mAh/g . The discharge capacity of ND27 is 300.5 mAh/g . Compared with that of natural samples, the discharge capacity of thermal simulated samples is lower.

As shown in Figure 12, the thermal conductivity of the artificially graphitized sample decreased gradually with the increase of the graphitization temperature. The thermal conductivity of the graphitization temperature was the lowest 1.21 W/(m K) at 1800°C and the highest 4.06 W/(m K) at 2700°C . At the same degree of graphitization. The thermal

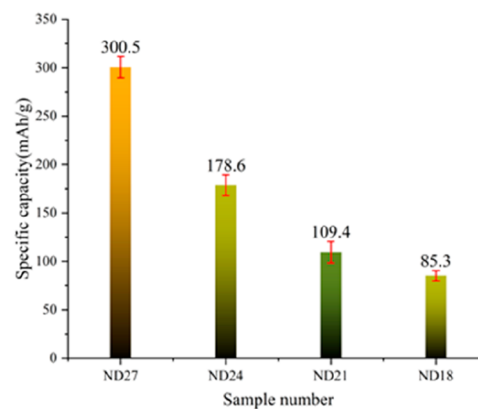


Figure 11. Thermal simulation samples discharge capacity histogram.

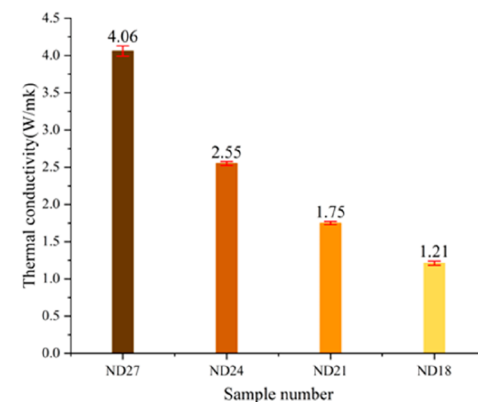


Figure 12. Thermal simulation samples thermal conductivity histogram.

conductivity of artificially simulated samples is lower than that of naturally evolved samples

4. DISCUSSION

In this study, from the perspective of macromolecular structure evolution, linear fitting was conducted to establish the correlations between the microcrystalline parameters (d_{002} , L_a , and L_c) and the impedance, discharge-specific capacity, and thermal conductivity.

4.1. Graphitization Degree and Physical Properties of Natural Evolution Samples.

4.1.1. Impedance. By analyzing the scatter plot of d_{002} -impedance (Figure 13), it can be concluded that the sample's impedance gradually decreases with an increase in the graphitization degree, leading to an increase in electrical conductivity.

According to the scatter plot, the electrical conductivity enhancement in the samples can be divided into three stages. First, in the anthracite stage (Z10–Z9), the sample impedance remains unchanged, and the electrical conductivity remains unchanged during the coalification process. In the transition from the anthracite to semigraphite stage (Z8–Z6), the impedance of the sample decreases, and the electrical conductivity begins to increase significantly. In the transition from the semigraphite to the graphite stage (Z5–Z1), the impedance of the sample decreases sharply, leading to an explosive increase in electrical conductivity.

Analysis of the scatter plots of L_a -impedance and L_c -impedance (Figure 14) reveals a negative linear correlation between the impedance and the degrees of stacking and

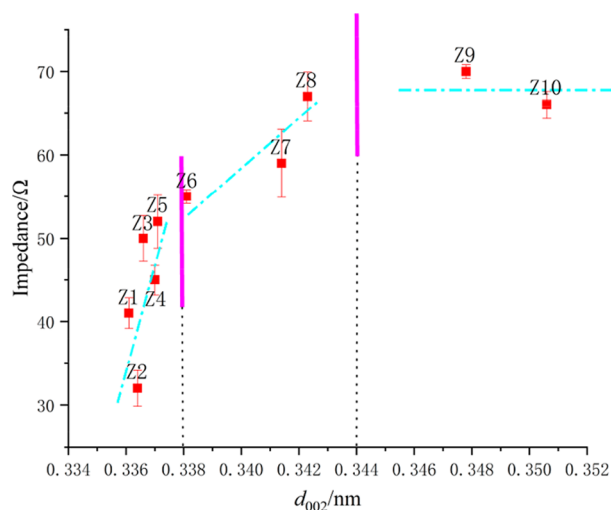


Figure 13. Scatter diagram of d_{002} and impedance.

extension. The fitted line indicates that L_a and L_c exhibit a good linear relationship with impedance. The correlation coefficient R^2 of the linear fitting between L_a and impedance is 0.93. The correlation coefficient R^2 of linear fitting between L_c and impedance is 0.88. The impedance is directly affected by the microcrystalline parameters and increases linearly with the increases in L_a and L_c .

4.1.2. Specific Capacity of Initial Discharge. By analysis of the scatter plot depicting the relationship between the initial discharge-specific capacity and the graphite microcrystalline layer spacing (d_{002}) (Figure 15), it is evident that the discharge capacity gradually decreases with an increase in the sample microcrystalline layer spacing (d_{002}). This negative correlation indicates that as the degree of graphitization increases, the initial discharge-specific capacity increases.

According to the scatter diagram, the specific capacity growth during discharge can be divided into three stages. In the anthracite stage (Z10–Z8), the specific capacity growth during the initial discharge of the sample is very slow, almost negligible. This is because the structure of the sample undergoes minimal changes during this stage; in the later stage of coalification, the removal of organic matter is still ongoing, which does not significantly increase the specific capacity of the initial discharge, and there are still a lot of defects and irregular structures in the sample. When the microcrystalline layer spacing is between 0.338 and 0.344 nm,

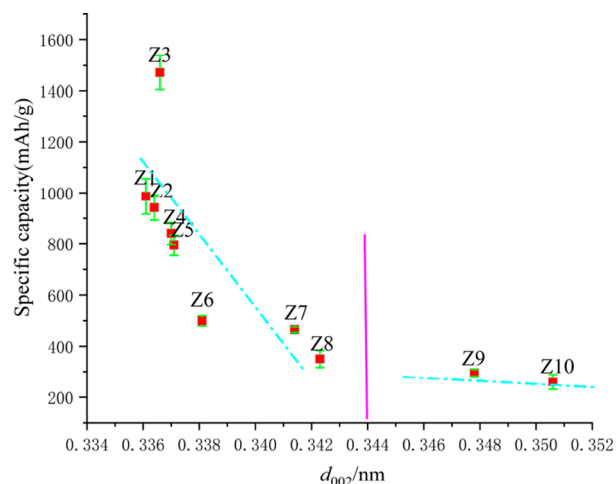


Figure 15. Scatter diagram of d_{002} and discharge capacity.

the specific discharge capacity of the sample starts to increase significantly, corresponding to the semigraphite to graphite phase (Z8–Z6) and exhibits almost linear growth. The specific discharge capacity continues to increase steadily in the graphite stage (Z5–Z1), corresponding to $d_{002} < 0.338$ nm, with a growth rate similar to the previous stage but with a smaller increment. This is because the d_{002} value is a capacity determining parameter, and the effects of L_a and L_c on its capacity are less important.³¹

4.1.3. Thermal Conductivity. The correlation between d_{002} and thermal conductivity is depicted in the scatter plot (Figure 16). It can be observed that the thermal conductivity of the sample increases with an increase in the degree of graphitization. In the anthracite and semigraphite phases (from Z10 to Z6), the increase in the thermal conductivity is relatively slow. However, when $d_{002} < 0.338$ nm, in the graphite stage (from Z5 to Z1), the thermal conductivity of the sample begins to increase significantly, with a growth rate much higher than that of the previous stage.

It can be observed from the scatter plot between the L_a –thermal conductivity and L_c –thermal conductivity that the microcrystalline parameters L_a and L_c have a certain correlation with thermal conductivity and linear fitting, respectively. As shown in Figure 17, the correlation coefficient R^2 of linear fitting between L_a and thermal conductivity is 0.82, and the

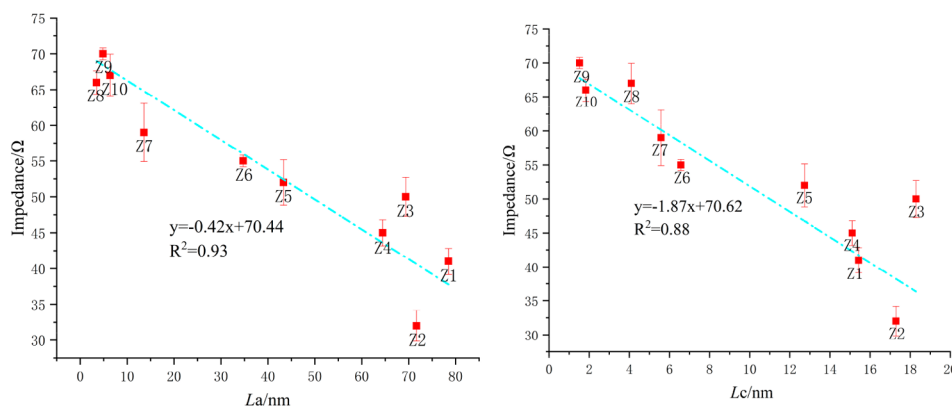


Figure 14. Scatter plot of L_a and impedance (left); scatter plot of L_c and impedance (right).

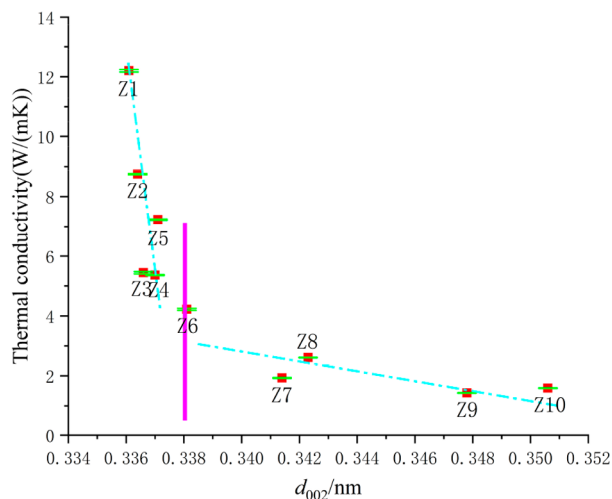


Figure 16. Scatter diagram of d_{002} and thermal conductivity.

correlation coefficient R^2 of linear fitting between L_c and thermal conductivity is 0.84.

4.2. Relationship between Graphitization Degree and Physical Properties of the Thermally Simulated Samples. The relationship between graphitization degree and physical properties of artificially simulated graphitized samples is the same as that of naturally evolved samples; the physical properties increased with the increase of graphitization degree (Figure 18), but at the same degree of graphitization are lower than those of natural samples, that is, higher impedance, lower discharge capacity, and lower thermal conductivity. This is due to the natural evolution of the sample not only after a long time of geothermal heating, but also continuous stress,¹² which makes the graphite crystal growth more complete, with more complete L_a and L_c and stronger physical properties.

4.3. Mechanism of Macromolecular Structure Evolution on Physical Properties. The impedance is the internal resistance of the battery, which can reflect the ability to conduct ions to pass through. A smaller impedance indicates a higher ion conductivity and stronger electrical conductivity. The electrical conductivity of graphite is primarily dependent on the total concentration of conducting carriers within the

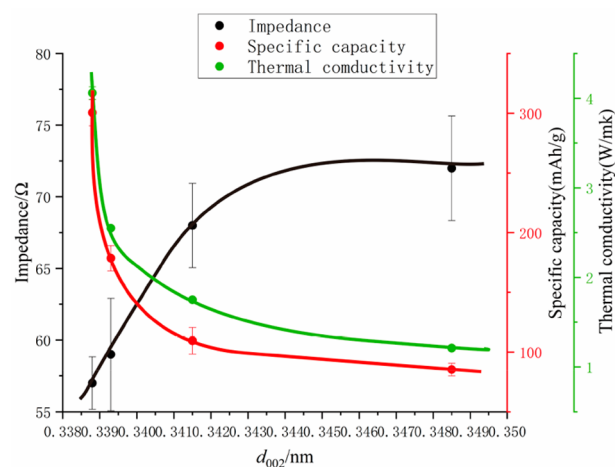


Figure 18. Scatter diagram of thermal simulation sample d_{002} and physical properties.

lattice and the free movement of carriers. It determines whether electrons can circulate within the material. The electrical conductivity of graphite in the direction of the parallel plane is much greater than that in the vertical plane. A comprehensive analysis of the scatter plot and the fitting line shows that there is a strong correlation between the impedance of the sample and microcrystalline parameters. In the anthracite stage, the electrical conductivity remains unchanged. This could be attributed to the fact that the coal structure has not transformed into graphite or still contains a significant amount of H and O during the removal of organic matter, which hinders electron migration and results in poor electrical conductivity. The electrical conductivity is obviously enhanced at the anthracite to semigraphite stage. At this stage, the deoxygenation and dehydrogenation process is basically complete, and the organic matter in the sample gradually disappears, leading to an improvement in conductivity. However, when the degree of graphitization is low, graphite crystals in this stage are primarily ordered in a 2D plane with a less 3D crystalline structure. At the same time, there are structural defects in this process, and there are many disordered structures in the sample, resulting in a slow rate

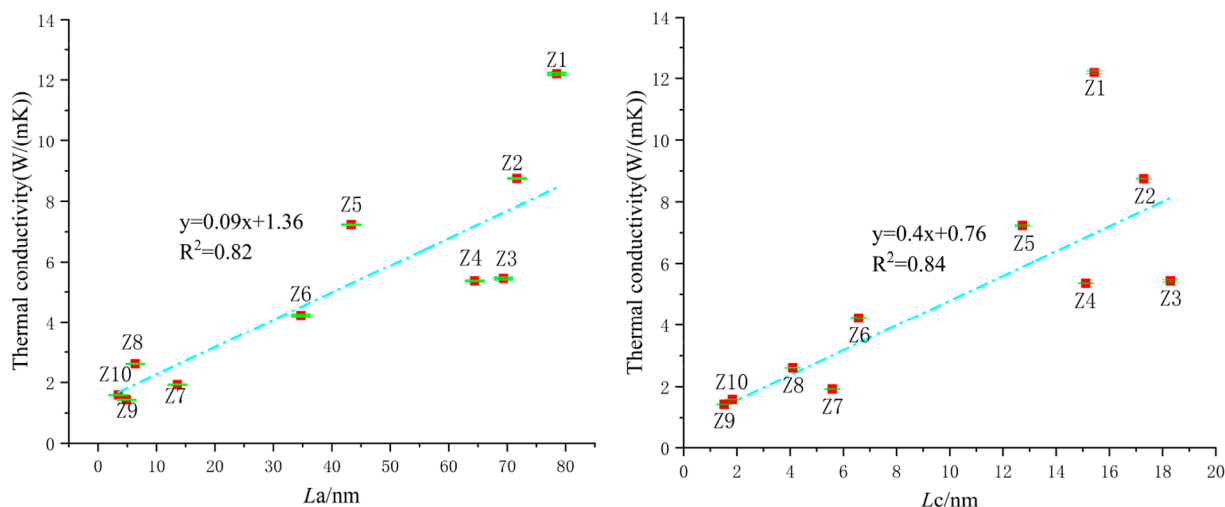


Figure 17. Scatter diagram of L_c and thermal conductivity

of electrical conductivity enhancement. At the semigraphite to graphite stage, the electrical conductivity begins to increase explosively. At this stage, the defects in the samples are almost repaired. With the progress of graphitization, the degree of stacking and elongation begins to increase significantly, providing a good channel for electrons and greatly improving the electrical conductivity. It can be seen from SG that the impedance difference between the cryptocrystalline graphite and the graphite sample is not very obvious, which means that when the graphitization reaches the ideal state, that is, the end point of evolution graphite, the electrical conductivity reaches the maximum and reaches the level of graphite. As shown in Figure 19, when the stacking and extension degree of the

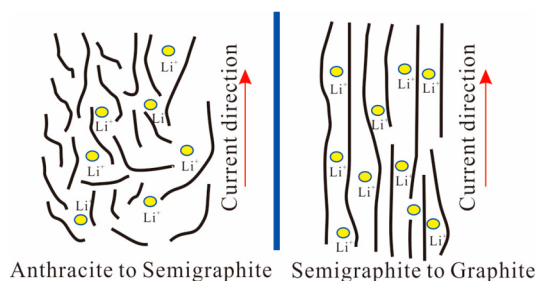


Figure 19. Schematic diagram of electronic circulation.

sample increase, the internal structure is stacked in layers, which greatly reduces the obstruction of electron passage and significantly enhances the electrical conductivity. However, when the degree of stacking and elongation is low, there are more disordered structures in the sample, which leads to the obstruction of electron flow and a decrease in the sample conductivity.

Comparing SG and natural evolution samples, it can be seen that coal-based cryptocrystalline graphite has a lithium storage capacity much higher than that of SG, because mostly cryptocrystalline graphite is micrystalline disordered carbon. For this kind of disordered carbon with a small grain size, the lithium intercalation mechanism mainly involves surface adsorption or edge lithium storage. This implies that lithium ions are not only inserted in the graphite layer but also doped on the surface and edge of graphite. The surface and edge of graphite have more lithium ions than interlayer doping, allowing this type of carbon material to have a lithium storage capacity several times more than the theoretical capacity of graphite.^{56,57} However, graphite has a complete crystal structure, and lithium ions are mainly stored between carbon layers, which lead to certain limitations in its lithium storage capacity. During charging, lithium ions migrate from the lithium sheet under the action of voltage, pass through the diaphragm to the graphite electrode in the electrolyte, insert into the graphite layer, and adsorb on its surface. Lithium ions leave the graphite electrode during discharge and return to the lithium sheet to form a stable current. In the first few charging cycles of the liquid lithium-ion battery, the electrolyte is decomposed on the graphite positive electrode and the lithium sheet through an interfacial reaction to produce a layer of solid electrolyte interfacial phase (SEI)^{58,59} (Figure 20). The SEI acts as a passivation layer on the surface of the electrode, blocking electrons and allowing lithium ions to pass through. This prevents further decomposition of electrons and electrolytes and ensures long-term cycles.^{60–62} However, the SEI film

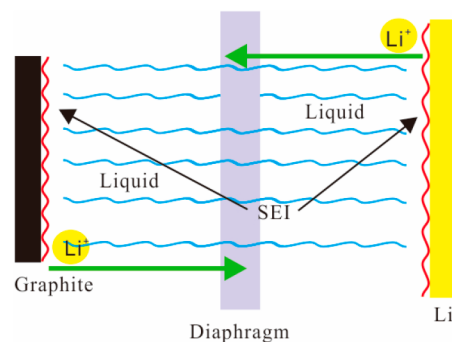


Figure 20. Mechanism of SEI membrane action.

can also absorb some lithium ions during the lithium-ion transmission process, which leads to a reduction of the specific discharge capacity.

The specific capacity of the first discharge increases gradually with the increase of the degree of graphitization. As the defects of the sample begin to repair and the impurities are reduced, the side reaction of the first film formation is reduced, the SEI passivation layer is thinner, and more lithium ions are released during the ion transport process, and the specific discharge capacity is increased. In addition, the increase of graphitization degree also leads to the increase of microcrystalline size, the graphite particle size becomes larger so that it has a smaller specific surface area, and the formed SEI passivation film consumes less lithium ions. At the same time, the larger microcrystalline size provides more lithium storage space and improves the specific capacity of the first discharge.⁶³ When the graphite stage is reached, the graphitization makes the L_a and L_c of the sample begin to increase significantly, the impedance of the sample begins to be greatly reduced, the ion pass rate is improved, the lithium ion diffusion power is greatly increased, the lithium ion de-embedding amount is also increased to a certain extent, and the specific capacity of the first discharge is increased.

A comprehensive analysis of the scatter plot and the fitted linear equation shows that there is a strong correlation between the thermal conductivity of the sample and the lattice parameters, where the thermal conductivity increases with the growth of the lattice. This is because heat transfer primarily occurs through radiation, convection, or conduction. In all solid materials, heat conduction is realized by thermal vibration of lattice atoms and the flow of free electrons. For most metals, the heat conduction of free electrons is the main one. For nonmetals of carbon and graphite products, the heat conduction mechanism mainly relies on the nonharmonic vibration of elastic lattice (i.e., the interaction of phonons) to transfer heat.^{64–66} Phonon thermal conductivity can be calculated from the Makinson equation:

$$\lambda = 3n\bar{V}R\left(\frac{T}{\Theta}\right)^3 \int_0^{T/\Theta} \frac{\xi^4 e^{\xi} L(\xi T, T)}{(e^{\xi} - 1)^2} d\xi \quad (6)$$

$\xi = h\omega/kT$; \bar{V} is the average speed of phonon motion; L is the free path of phonons; k is the Boltzmann constant; R is the universal gas constant; h is Planck's constant; ω is the frequency; and Θ is the Debye temperature. The main factors affecting λ are the mean velocity \bar{V} of phonon motion and the free path L of phonon. Various defects, namely, discontinuous points (such as dislocation, point defects, and grain boundaries), will lead to irregular structure and hinder phonon

propagation, resulting in scattering.⁶⁷ It can be seen from the thermal conductivity of SG that graphite, as a crystalline mineral, has a very high degree of crystal integrity and structural order compared with the transitional mesophase of cryptocrystalline graphite, and there is also a certain amount of disordered organic components in cryptocrystalline graphite, making graphite have higher thermal conductivity than cryptocrystalline graphite. Although the thermal conductivity of human simulated graphitization also increases with the increase of the degree of graphitization, the artificial conditions cannot simulate natural geological evolution, resulting in microcrystalline structure parameters of the samples simulated by artificial thermal simulation not being as complete as those of the natural samples, making their thermal conductivity low. With the increase of graphitization degree, the distance between the crystal surface layers of the microcrystals decreases, the lattice defects in the graphite materials reduce, the arrangement of the microcrystals gradually becomes more regular and the factors affecting phonon scattering weaken. At the same time, the reduction of defects and the increase in grain size will increase the average speed \bar{V} of phonons and the free path L . Consequently, the thermal conductivity of the materials increases. Figure 21 shows the phonon vibration

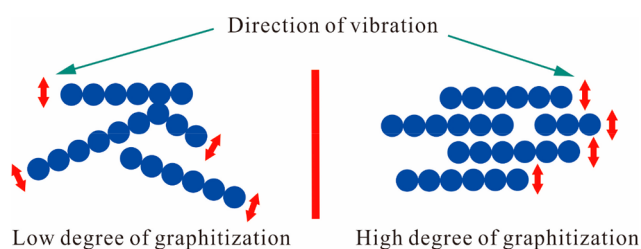


Figure 21. Phonon vibration modes with different degrees of graphitization.

modes with different degrees of graphitization. As the degree of graphitization increases, the arrangement of C layers gradually becomes orderly and the direction of phonon vibration tends to be consistent. When the degree of graphitization is low due to a certain angle of arrangement between C layers, part of the phonon vibration energy escapes in the horizontal direction, and the average speed and free path of phonons are low, resulting in reduced energy transmission efficiency and poor thermal conductivity. However, when the degree of graphitization increases, the arrangement of C layers tends to be parallel, the vibration direction of phonons moves only in the direction perpendicular to the layer, the energy loss is minimal, and the average speed and free path of phonons are large. These greatly improve the energy transmission efficiency and thus improve the thermal conductivity.

5. CONCLUSION

(1) Electrical conductivity increases with the increase in graphitization degree, and the growth rate gradually increased. The impedance decreases almost linearly with the increase of L_a . The fitted linear equation is $y = -0.42x + 70.44$, and the correlation coefficient reaches 0.93. The impedance decreases almost linearly with the increase of L_c and the linear fitting equation between them is $y = -1.87x + 70.62$, the correlation coefficient is 0.88. As the graphitization degree increases, the degree of stacking and elongation increases, the arrangement of the C layers is gradually ordered, the obstruction of conductive

ions passing through is greatly reduced, impedance is reduced, and the conductivity is enhanced.

(2) With the increase of graphitization degree, the initial specific discharge capacity gradually increased. As the defects of the sample began to be repaired, the microcrystal size began to become larger, which reduced the side reaction of the first film formation and the consumption of lithium ions during the film formation process, and the initial specific discharge capacity increased. At the same time, the larger microcrystal size provides more storage space for lithium, improving the specific capacity of the first discharge. The low impedance of the high graphitization stage can provide more power for ion diffusion and increase the specific capacity of the first discharge.

(3) The thermal conductivity gradually increases with an increase in the degree of graphitization, the growth rate gradually increases, and the growth rate changes obviously when $d_{002} = 0.338$ nm. The linear equation of L_a and thermal conductivity is $y = 0.09x + 1.36$, and the correlation coefficient reaches 0.82. The linear equation of L_c and thermal conductivity is $y = 0.4x + 0.76$, and the correlation coefficient is 0.84. This is due to the reduction in defects and the regularity of C-layer arrangement, resulting in a great reduction in phonon vibration energy escape and improved energy transfer efficiency, and at the same time, the average speed and free path of phonons increase, enhancing thermal conductivity.

(4) The physical properties of artificially simulated graphitized samples and naturally evolved graphite samples increased with the increase of graphitization degree. However, the physical properties of the thermal simulated samples are generally lower than those of the natural evolution samples. Because the artificial thermal simulation only goes through a short period of high temperature, its graphitization degree can only reach semigraphite at the highest. However, the natural evolution samples go through a long period of high temperature and high pressure under geological conditions; not only its graphitization degree can reach a higher level but also the graphite microcrystalline parameters are more complete. The physical properties of the samples are higher than those of the graphitized samples under artificial conditions.

(5) By comparing the experimental data of graphite and cryptocrystalline graphite, it can be seen that the conductive property of cryptocrystalline graphite is smaller than that of graphite and it can be used as a secondary substitute for graphite in conductive component applications to alleviate the pressure on the demand for graphite resources. In terms of electrochemical energy storage, cryptocrystalline graphite has the advantage of higher reserves than graphite, which can provide a new direction for the selection of energy storage materials. In terms of thermal conductivity, due to its own limitations, there is still a certain gap between the thermal conductivity of cryptocrystalline graphite and graphite, and the traditional graphite (graphene) has more unique advantages in the application of thermal interface materials.

■ ASSOCIATED CONTENT

Supporting Information

The Supporting Information is available free of charge at <https://pubs.acs.org/doi/10.1021/acsomega.3c06871>.

Table S1 showing experimental results data (PDF)

AUTHOR INFORMATION

Corresponding Author

Daiyong Cao – College of Geoscience and Surveying Engineering, China University of Mining and Technology, Beijing 100083, China; State Key Laboratory of Coal Resources and Safe Mining, China University of Mining and Technology, Beijing 100083, China; orcid.org/0000-0003-3065-426X; Email: cdy@cumtb.edu.cn

Authors

Xiang Xu – College of Geoscience and Surveying Engineering, China University of Mining and Technology, Beijing 100083, China; orcid.org/0009-0001-5718-0511

Yingchun Wei – College of Geoscience and Surveying Engineering, China University of Mining and Technology, Beijing 100083, China; State Key Laboratory of Coal Resources and Safe Mining, China University of Mining and Technology, Beijing 100083, China; orcid.org/0000-0002-8900-8951

Anmin Wang – College of Geoscience and Surveying Engineering, China University of Mining and Technology, Beijing 100083, China; State Key Laboratory of Coal Resources and Safe Mining, China University of Mining and Technology, Beijing 100083, China; orcid.org/0000-0001-7275-8871

Gaojian Chen – College of Geoscience and Surveying Engineering, China University of Mining and Technology, Beijing 100083, China

Tianyuan Wang – School of Chemical and Environmental Engineering, China University of Mining and Technology, Beijing 100083, China

Guixiang Wang – Henan Geological Bureau, China Chemical Geology and Mine Bureau, Zhengzhou 450000 Henan, China

Xinli Chen – Henan Geological Bureau, China Chemical Geology and Mine Bureau, Zhengzhou 450000 Henan, China

Complete contact information is available at:
<https://pubs.acs.org/10.1021/acsomega.3c06871>

Author Contributions

X.X.: Experimental design, experimental testing, data analysis, and writing. C.D.: Methods and ideas, revised manuscripts, resources, and supervision. W.A.: Modification of manuscripts and supervision. C.G.: Methods and ideas. W.T.: Experimental testing. W.G.: Provision of samples. C.X.: Provision of samples.

Notes

The authors declare no competing financial interest.

ACKNOWLEDGMENTS

This study was financially supported by the National Natural Science Foundation of China (Grant Nos. 42072197, 41902170, and 41972174).

REFERENCES

- (1) Zhao, X.; Li, W.; Wang, Y.; Li, H.; Wang, J. Bioinspired modified graphite film with superb mechanical and thermoconductive properties. *Carbon* **2021**, *181*, 40–47.
- (2) Guo, R.; Li, W.; Han, Y. Progress on the separation, purification and application of natural graphite. *Huagong Jinzhan* **2021**, *40* (11), 6155–6172.
- (3) Zhu, W.; Kang, J.; Zhang, D. Research status of metallogenic regularity and flotation technology of graphite resources. *Kuangwu Xuebao* **2023**, *43* (3), 1–22.
- (4) The Role of Critical Minerals in Clean Energy Transitions, Paris, May 2021; IEA: Paris, 2021. See related report: <https://www.iea.org/reports/the-role-of-critical-minerals-in-clean-energy-transitions>.
- (5) Quan, Y.; Liu, Q.; Zhang, S.; Zhang, S. Comparison of the morphology, chemical composition and microstructure of cryptocrystalline graphite and carbon black. *Appl. Surf. Sci.* **2018**, *445*, 335–341.
- (6) Cao, D.; Wang, L.; Liu, Z.; Din, Z.; Li, Y.; Shu, Z. The research status and prospect of coal-based graphite in China. *Coal Geol. Explor.* **2020**, *48* (1), 1–11.
- (7) Cao, D.; Zhang, H.; Dong, Y.; Wu, G.; Ning, S.; Mo, J.; Li, X. Research status and key orientation of coal-based graphite mineral geology. *Earth Sci. Front.* **2017**, *24* (05), 317–327.
- (8) Cao, D.; Li, X.; Zhang, S. Influence of tectonic stress on coalification: Stress degradation mechanism and stress polycondensation mechanism. *Sci. China D* **2007**, *50* (1), 43–54.
- (9) Marqués, M.; Suárez-Ruiz, I.; Flores, D.; Guedes, A.; Rodrigues, S. Correlation between optical, chemical and micro-structural parameters of high-rank coals and graphite. *Int. J. Coal Geol.* **2009**, *77* (3–4), 377–382.
- (10) Kwiecińska, B.; Petersen, H. Graphite, semi-graphite, natural coke, and natural char classification—ICCP system. *Int. J. Coal Geol.* **2004**, *57* (2), 99–116.
- (11) Li, K.; Liu, Q.; Song, B.; Zhang, S.; Wu, Y. Investigation on structural evolution and thermal reaction of coal-based graphite from Xinhua County, Hunan Province. *Coal Geol. Explor.* **2020**, *48* (01), 42–47.
- (12) Cao, D.; Zhang, H.; Dong, Y.; Yang, C. Nanoscale microscopic features and evolution sequence of coal-based graphite. *J. Nanosci. Nanotechnol.* **2017**, *17* (9), 6276–6283.
- (13) Li, H.; Liu, W.; Lu, J.; Lu, Y.; Shi, S.; Wang, Z.; Ye, Q.; Jia, Z. Effect of microwave-assisted acidification on the microstructure of coal: XRD, 1H, NMR, and SEM studies. *Int. J. Min. Sci. Technol.* **2023**, *33* (7), 919–926.
- (14) Zeng, H.; Xing, B.; Cao, Y.; Xu, B.; Hou, L.; Guo, H.; Cheng, S.; Huang, G.; Zhang, C.; Sun, Q. Insight into the microstructural evolution of anthracite during carbonization-graphitization process from the perspective of materialization. *Int. J. Min. Sci. Technol.* **2022**, *32* (6), 1397–1406.
- (15) Cao, D.; Wei, Y.; Li, Y.; Liu, Z.; Li, H.; Wang, L.; Wu, G.; Ning, S.; Xu, X. Determination of identification index and construction of classification and classification system of coal measures graphite. *China Coal Soc.* **2021**, *46* (6), 1833–1846.
- (16) Cao, D.; Wang, L.; Zhu, W.; Wu, G.; Wei, Y.; Ning, S.; Wang, Xiao, J.; Xu, X.; Liu, K. Discussion on identification standard of coal-measure graphite. *Coal Geol. Explor.* **2022**, *50* (12), 105–113.
- (17) Chen, H.; Wang, S.; Zhang, X.; Zhao, Y.; Zhang, H. A study of chemical structural evolution of thermally altered coal and its effect on graphitization. *Fuel* **2021**, *283*, 119295.
- (18) Moura, H.; Suárez-Ruiz, I.; Marques, M.; Ribeiro, J.; Cunha, P.; Flores, D. Influence of magmatic fluids on the organic and inorganic fractions of coals from the Peñarroya-Belmez-Espiel Basin (Spain). *Int. J. Coal Geol.* **2021**, *235*, 103679.
- (19) Wang, L.; Cao, D.; Peng, Y.; Ding, Z.; Li, Y. Strain-induced graphitization mechanism of coal-based graphite from Lutang, Hunan province, China. *Minerals* **2019**, *9* (10), 617.
- (20) Gong, J.; Wu, H. Electrochemical intercalation of lithium species into disordered carbon prepared by the heat-treatment of poly(p-phenylene) at 650°C for anode in lithium-ion battery. *Electrochim. Acta* **2000**, *45* (11), 1753–1762.
- (21) Xing, W.; Wilson, A.; Zank, G.; Dahn, J. Pyrolysed pitch-polysilane blends for use as anode materials in lithium ion batteries. *Solid State Ionics* **1997**, *93* (3–4), 239–244.
- (22) Endo, M.; Kim, C.; Karaki, T.; Fujino, T.; Matthews, M.J.; Brown, S.D.M.; Dresslhaus, M.S. In situ Raman study of PPP-based

- disordered carbon as an anode in a Li ion battery. *Synth. Met.* **1998**, *98* (1), 17–24.
- (23) Zhou, Q.; Wen, B.; Xie, Z. Microcrystalline graphite modified as lithium-ion battery anode material. *J. Funct. Mater.* **2023**, *54* (2), 2167–2173.
- (24) Sole, C.; Drewett, N.; Hardwick, L. In situ Raman study of lithium-ion intercalation into microcrystalline graphite. *Faraday Discuss.* **2014**, *172*, 223–237.
- (25) Kim, K.; Lee, T.; Kim, H.; Lim, S.; Lee, S. A hard carbon/microcrystalline graphite/carbon composite with a core-shell structure as novel anode materials for lithium-ion batteries. *Electrochim. Acta* **2014**, *135*, 27–34.
- (26) Liao, L.; Yi, W.; Ye, Y. Influence of graphitization temperature on the microstructure and electrochemical properties of artificial graphite. *Tansu Jishu* **2023**, *42* (1), 46–50.
- (27) Yang, Z.; Bao, C.; Chen, Y.; Xia, X.; He, Y. Effect of heat treatment temperature on structure and electrochemical properties of needle coke. *Tansu Jishu* **2022**, *41* (2), 45–52.
- (28) Ghosh, A.; Razzino, C. d. A.; Dasgupta, A.; Fujisawa, K.; Vieira, L. H. S.; Subramanian, S.; Costa, R. S.; Lobo, A. O.; Ferreira, O. P.; Robinson, J.; Terrones, M.; Terrones, H.; Viana, B. C. Structural and electrochemical properties of babassu coconut mesocarp-generated activated carbon and few-layer graphene. *Carbon* **2019**, *145*, 175–186.
- (29) Wang, G.; Qin, X.; Han, D.; Liu, Z. Study on seepage and deformation characteristics of coal microstructure by 3D reconstruction of CT images at high temperatures. *Int. J. Min. Sci. Technol.* **2021**, *31* (2), 175–185.
- (30) Guo, H. J.; Wang, K.; Wu, Y.; Tang, H.; Wu, J.; Guan, L.; Chang, C.; Xu, C. Evaluation of the weakening behavior of gas on the coal strength and its quantitative influence on the coal deformation. *Int. J. Min. Sci. Technol.* **2021**, *31* (3), 451–462.
- (31) Heckmann, A.; Fromm, O.; Rodehorst, U.; Münster, P.; Winter, M.; Placke, T. New insights into electrochemical anion intercalation into carbonaceous materials for dual-ion batteries: impact of the graphitization degree. *Carbon* **2018**, *131*, 201–212.
- (32) Lin, X.; Huang, J.; Zhang, B. Correlation between the microstructure of carbon materials and their potassium ion storage performance. *Carbon* **2019**, *143*, 138–146.
- (33) Tatsumi, K.; Iwashita, N.; Sakaebe, H.; Shioyama, H.; Higuchi, S.; Mabuchi, A.; Fujimoto, H. The influence of the graphitic structure on the electrochemical characteristics for the anode of secondary lithium batteries. *J. Electrochem. Soc.* **1995**, *142* (3), 716–720.
- (34) Zhao, L.; Tang, J.; Zhou, M.; Shen, K. A review of the coefficient of thermal expansion and thermal conductivity of graphite. *New Carbon Mater.* **2022**, *37* (3), 544–555.
- (35) Taylor, R. The thermal conductivity of pyrolytic graphite. *Philos. Mag.* **1966**, *13* (121), 157–166.
- (36) Nihira, T.; Iwata, T. Thermal resistivity changes in electron-irradiated pyrolytic graphite. *Jpn. J. Appl. Phys.* **1975**, *14* (8), 1099–1104.
- (37) Feser, J.; Cahill, D. Probing anisotropic heat transport using time-domain thermoreflectance with offset laser spots. *Rev. Sci. Instrum.* **2012**, *83* (10), 104901.
- (38) Jiang, P.; Qian, X.; Yang, R. Time-domain thermoreflectance (TDTR) -measurements of anisotropic thermal conductivity using a variable spot size approach. *Rev. Sci. Instrum.* **2017**, *88* (7), 074901.
- (39) Qian, X.; Ding, Z.; Shin, J.; Schmidt, A.; Chen, G. Accurate-basedment of in-plane thermal conductivity of layered materials without metal film transducer using frequency domain thermoreflectance. *Rev. Sci. Instrum.* **2020**, *91* (6), 064903.
- (40) Zhao, X.; Li, C.; Bai, K.; Xie, B.; Chen, J.; Liu, Q. Multiple structure graphite stabilized stearic acid as composite phase change materials for thermal energy storage. *Int. J. Min. Sci. Technol.* **2022**, *32* (6), 1419–1428.
- (41) Qiu, H.; Guo, Q.; Song, Y.; Zhai, G.; Song, J.; Liu, L. Study of the relationship between thermal conductivity and microcrystalline parameters of bulk graphite. *New Carbon Mater.* **2002**, *17* (1), 36–40.
- (42) Li, J.; Huang, Q.; Cao, H. Processing and application situation of amorphous graphite. *Tansu Jishu* **2021**, *40* (01), 9–14.
- (43) Rodrigues, S.; Marques, M.; Suárez-Ruiz, I.; Camean, I.; Flores, D.; Kwiecinska, B. Microstructural investigations of natural and synthetic graphites and semi-graphites. *Int. J. Coal Geol.* **2013**, *111*, 67–79.
- (44) Franklin, R. E. Crystallite growth in graphitizing and non-graphitizing carbons. *Proc. R. Soc. London A* **1951**, *209* (1097), 196–218.
- (45) Chen, W. About the graphitization degree calculation formula. *Tansu Jishu* **1983**, No. 06, 28–31.
- (46) Wang, L.; Rahamim, G.; Vudutta, K.; Leifer, N.; Elazari, R.; Behar, I.; Noked, M.; Zitoun, D. Influence of the halogen in argyrodite electrolytes on the electrochemical performance of all-solid-state lithium batteries. *Energy Technol.* **2023**, *11* (3), 2201116.
- (47) Zhang, L.; Wang, Z.; Zhou, H.; Li, X.; Liu, Q.; Wang, P.; Yuan, A. Synergistic coupling of Li₆. 4La₃Zr₁. 4Ta₀. 6O₁₂ and fluoroethylene carbonate boosts electrochemical performances of poly (ethylene oxide)-based all-solid-state lithium batteries. *ChemElectroChem* **2022**, *9* (17), No. e202200641.
- (48) Saleem, A.; Majeed, M.; Iqbal, R.; Hussain, A.; Naeem, M.; Rauf, S.; Wang, Y.; Javed, M.; Shen, J. Nitrogenized 2D covalent organic framework decorated Ni-Rich single crystal cathode to ameliorate the electrochemical performance of lithium batteries. *Adv. Mater. Interfaces* **2022**, *9* (27), 2200800.
- (49) Lu, Z.; Tai, Z.; Yu, Z.; LaGrow, A.; Bondarchuk, O.; Sousa, J.; Meng, L.; Peng, Z.; Liu, L. Lithium-copper alloy embedded in 3D porous copper foam with enhanced electrochemical performance toward lithium metal batteries. *Mater. Today Energy* **2021**, *22*, 100871.
- (50) Ge, Y.; Yang, D.; Gao, C.; Han, J.; Tian, X.; Gao, J.; Hu, G.; Lu, H. Research progress of high thermal conductivity graphene composites. *Shanghai Suliao* **2022**, *50* (5), 1–7.
- (51) Jin, D.; Lu, Y.; Yu, Y.; Chen, F.; Lin, Y.; Li, R.; Wang, Z.; Lin, X.; Guan, C.; Wang, J. Application of electrochemical impedance spectroscopy in solid oxide fuel cells. *Mater. Res. Appl.* **2023**, *17* (2), 220–233.
- (52) Wang, L.; Qin, R.; Li, Y.; Zhang, H. On the difference of graphitization behavior between vitrinite-and inertinite-rich anthracites during heat treatment. *Energy Sources, Part A* **2022**, *44* (2), 4991–5003.
- (53) Chen, G.; Cao, D.; Wang, A.; Wei, Y.; Liu, Z.; Zhao, M. A High-Temperature Thermal Simulation Experiment for Coal Graphitization with the Addition of SiO₂. *Minerals* **2022**, *12* (10), 1239.
- (54) Liu, Z.; Cao, D.; Chen, G.; Chen, Q.; Bi, Z. High-temperature graphitization characteristics of vitrinite and inertinite. *Front. Earth Sci.* **2023**, *11*, 1235457.
- (55) Liu, Z.; Cao, D.; Chen, G.; Bi, Z.; Chen, Q. Experimental Verification for the Graphitization of Inertinite. *Minerals* **2023**, *13* (7), 888.
- (56) Wang, S.; Matsumura, Y.; Maeda, T. A model of the interactions between disordered carbon and lithium. *Synth. Met.* **1995**, *71* (1–3), 1759–1760.
- (57) Matsumura, Y.; Wang, S.; Mondori, J. Interactions between disordered carbon and lithium in lithium ion rechargeable batteries. *Carbon* **1995**, *33* (10), 1457–1462.
- (58) Geronov, Y.; Schwager, F.; Muller, R. Film formation on lithium anode in propylene carbonate. *J. Electrochem. Soc.* **1982**, *129* (7), 1422.
- (59) Peled, E. The electrochemical behavior of alkali and alkaline earth metals in nonaqueous battery systems—the solid electrolyte interphase model. *J. Electrochem. Soc.* **1979**, *126* (12), 2047–2051.
- (60) Li, S.; Huang, J.; Cui, Y.; Liu, S.; Chen, Z.; Huang, W.; Li, C.; Liu, R.; Fu, R.; Wu, D. A robust all-organic protective layer towards ultrahigh-rate and large-capacity Li metal anodes. *Nat. Nanotechnol.* **2022**, *17* (6), 613–621.

(61) Heiskanen, S.; Kim, J.; Lucht, B. Generation and evolution of the solid electrolyte interphase of lithium-ion batteries. *Joule*. **2019**, *3* (10), 2322–2333.

(62) Zhang, Z.; Li, L.; Zhu, Z.; Peng, W.; Li, Y. Study on impedance changes of SEI forming process. *Dianchi Gongye* **2020**, *24* (6), 288–291.

(63) Yang, Z.; Bao, C.; Chen, Y.; Xia, X.; He, Y.; Liu, H. Effect of heat treatment temperature on structure and electrochemical properties of needle coke. *Tansu Jishu* **2022**, *41* (2), 45–52.

(64) Lee, J.; Lee, S.; Choi, C.; Jang, S.; Choi, S. A review of thermal conductivity data, mechanisms and models for nanofluids. *Int. J. Micro-Nano Scale Transp.* **2010**, *1* (4), 269–322.

(65) Kotia, A.; Borkakoti, S.; Deval, P.; Ghosh, S. Review of interfacial layer's effect on thermal conductivity in nanofluid. *Heat Mass Transfer* **2017**, *53* (6), 2199–2209.

(66) Burger, N.; Laachachi, A.; Ferriol, M.; Lutz, M.; Toniazzi, V.; Ruch, D. Review of thermal conductivity in composites: Mechanisms, parameters and theory. *Prog. Polym. Sci.* **2016**, *61*, 1–28.

(67) Li, P.; Ma, L.; Xie, E.; Ren, Z.; Zhou, X.; Gao, H.; Wu, J. Crystal structure, thermal conductivity mechanism and surface modification of high thermal conductivity hexagonal boron nitride nanomaterials. *Mater. Rep.* **2022**, *36* (6), 44–55.